DISPERSION AT LOW AND HIGH PECLET NUMBERS IN FINITE-LENGTH PATTERNED MICROCHANNELS

Adrover A.
Dipartimento di Ingegneria Chimica, Materiali e Ambiente,
Sapienza, University of Rome,
Rome, 00184,
Italy,
E-mail: alessandra.adrover@uniroma1.it

NOMENCLATURE

D	[m^2/s]	Diffusion coefficient
D_{eff}	[-]	Effective dispersion coefficient
L	[m]	Channel length
$m^{(n)}$	[-]	n-th order temporal local moments
$m_{\text{out}}^{(n)}$	[-]	n-th order average outlet moments
$P^* = (P - P_{\text{out}})/(\rho_f U^2)$	[-]	Dimensionless pressure
P_{out}	[atm]	Outlet pressure
$Pe_{\text{ax}} = UL/D$	[-]	Axial Peclet number
$Pe_R = UR/D$	[-]	Cross-sectional Peclet number
$Re_R = \rho_f UR/\mu$	[-]	Reynolds number based on R
U	[m/s]	Average axial velocity
v_ζ^*, v_ρ^*	[-]	Dimensionless axial and radial velocities
r, z	[m]	Radial and axial coordinates

Special characters

$\alpha = L/R$	[-]	Channel aspect ratio
$\eta = l_w/l_s$	[-]	Pillar length over gap length
γ	[-]	Slip length
$\Gamma_{TA} = (192\,(1+4\gamma)^2)^{-1}$	[-]	Taylor-Aris dispersion coefficient
ϕ	[-]	Dimensionless solute concentration
$\chi = R/l_s$	[-]	Channel radius over gap length
ρ_f	[Kg/m^3]	Fluid density
σ_{out}^2	[-]	Variance of outlet chromatogram
$\tau = tU/L$	[-]	Dimensionless time
ζ, ρ	[-]	Dimensionless axial and radial coordinates

ABSTRACT

The present work focuses on laminar dispersion of solutes in finite-length patterned microtubes. Dispersion is strongly influenced by axial flow variations caused by patterns of periodic pillars and gaps in the flow direction. We focus on the Cassie Baxter state where the gaps are filled with with air pockets and thus free-slip boundary conditions apply at the liquid-air interface.

The analysis of dispersion in a finite-length microtube is approached by considering the temporal moments of solute concentration. With this approach it is possible to investigate the dispersion properties at low and high Peclet numbers and therefore how the patterned structure of the microtube influences both the Taylor-Aris and Convection-dominated dispersion regimes.

Numerical results for the velocity field and for the moment hierarchy are obtained by means of Finite Element Method (Comsol 3.5).

INTRODUCTION

How hydrodynamic dispersion is affected by wall slip remains to be fully understood. It was pointed out in many studies on slip flow in microchannels or microcapillaries that wall slippage would affect hydrodynamic dispersion [1]. The common thinking is that wall slip can reduce the cross-sectional velocity gradient, and therefore, will reduce the dispersion as well.

Dispersion is favourable in processes requiring enhanced mixing. However, it is undesirable for analytical techniques which require sharper resolution in terms of distinct peaks for constituent components [2].

Dispersion occurs through combined effects of advection and molecular diffusion. For a given diffusivity, dispersion depends only on the flow characteristics. Due to different flow characteristics, dispersion is sensitive to velocity profile, cross section of the conduit [3; 4], secondary flows that can suppress the dispersion through an enhanced transverse diffusion[5].

In this paper we investigate how dispersion is affected by axial flow variation caused by patterns of periodic pillars and gaps in flow direction. Such patterns occur naturally in superhydrophobic surfaces and may result from wall asperities or be fabricated purposefully in several microfluidic devices [6; 7]. Liquid placed over the pattern exists in two distinct limiting configurations: Cassie-Baxter and Wenzel state. Both flow features, i.e. slippage under Cassie state and recirculation/stagnant zones in Wenzel state, can potentially influence the transverse diffusion and dispersion.

We focus exclusively on the Cassie-Baxter state where the gaps are filled with with air pockets and thus free-slip boundary conditions apply at the liquid-air interface. The transition from a no-slip to a free slip boundary conditions (and viceversa) along the channel wall determines the presence of radial components of the velocity field (by fluid incompressibility) that should be accounted for in the solution, necessarily numerical, of the solute transport equation.

The analysis of dispersion in a finite-length channel is approached by considering the temporal moments of solute concentration and specifically the local temporal moments and the

average moments at the outlet of the flow channel[4]. With this approach it is possible to investigate the dispersion properties at low and high Peclet numbers.

Actually, for infinitely extended channels, i.e., whenever the characteristic axial length-scale is arbitrarily larger than the transverse linear size, Taylor-Aris theory [8] provides a complete description of the dispersion properties (at least for fully no-slip channels). However, whenever finite length channels are considered, new dispersion features arise, associated with dispersion regimes that deviate from the Taylor-Aris predictions, the so called *convection-dominated* dispersion regime [4]

We investigate how different dispersion regimes are influenced by the patterned structure of the microchannel. In particular we investigate the role of different geometrical parameters, namely $\alpha = L/R$ (channel aspect ratio, channel length L over channel radius R), $\eta = l_w/l_s$ (pillar length l_w over gap length l_s) and $\chi = R/l_s$ (channel radius over gap length), controlling the structure of the laminar velocity flow field.

The effects of geometry are analyzed by varying η and χ in the ranges $\eta \in [0.1-2]$ and $\chi \in [0.5-2]$ (typical ranges as encountered over lotus leaves) according with a preliminary and not conclusive work on dispersion in patterned microchannels by Bhaumik et al. [9].

Numerical results for the velocity fields and for the moment hierarchy are obtained by solving the Navier-Stokes equations and the transport equation for local moments by means of Finite-Element Method (Comsol 3.5). The incompressible Navier-Stokes and convection-diffusion packages in stationary conditions have been used. Lagrangian quadratic elements are chosen. The linear solver adopted is UMFPACK, with relative tolerance 10^{-12}. The number of finite triangular elements is $\simeq 10^6$ with a non-uniform mesh. Smaller elements have been located close to the boundaries between gaps and pillars (maximum element size of 1×10^{-3}). Adaptive mesh refinement i s adopted in order to guarantee (i) convergence of the numerical scheme and (ii) an accurate resolution of the boundary layer for local moments at high Pe_R values.

STATEMENT OF THE PROBLEM

Let us consider a cylindrical capillary of length L and radius R, aspect ratio $\alpha = L/R$. The flow is assumed to be under steady state with a parabolic inlet velocity profile. The presence of gaps of length l_s and pillars (length l_w) determines (i) axial flow variations and (ii) the presence of the radial velocity component.

The channel is characterized by an inlet and a outlet no-slip zones of length $2R$ ad by a periodic alternance of gaps (where slip boundary conditions apply) and pillars (where no slip boundary conditions apply), see Figure 1.

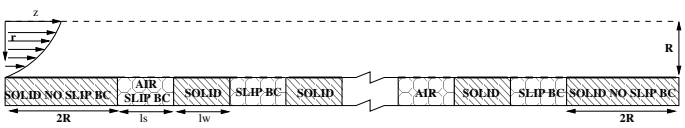

Figure 1. Patterned microchannel with $\chi = 1$, $\eta = 1$

By introducing the dimensionless quantities $\zeta = z/R$, $\rho = r/R$, $\mathbf{v}^* = \mathbf{v}/U$, $P^* = (P - P_{out})/(\rho_f U^2)$, $Re_R = \rho_f U R/\mu$, $\tilde{\nabla} = R\nabla$, $\tilde{\nabla}^2 = R^2\nabla^2$, U being the average velocity and P_{out} the outlet pressure, the Navier-Stokes equation attains the form

$$\tilde{\nabla} \cdot \mathbf{v}^* = 0\,, \quad \mathbf{v}^* \cdot \tilde{\nabla}\mathbf{v}^* = -\tilde{\nabla}P^* + \frac{1}{Re_R}\tilde{\nabla}^2\mathbf{v}^* \tag{1}$$

to be solved with (1) no slip boundary conditions on pillars ($\mathbf{v}^* = 0$), (2) slip boundary conditions on gaps

$$\mathbf{v}^* \cdot \mathbf{n} = 0\,, \quad \left(-P^*\mathbf{I} + \frac{1}{Re_R}(\tilde{\nabla}\mathbf{v}^* + (\tilde{\nabla}\mathbf{v}^*)^T)\right) \cdot \mathbf{n} = 0 \tag{2}$$

(3) axial symmetry boundary condition at $\rho = 0$, (4) inlet parabolic profile $\mathbf{v}^*(\zeta = 0, \rho) = (v^*_\zeta, v^*_\rho) = (2(1-\rho^2), 0)$ and (5) outlet pressure $P^* = 0$ at $\zeta = \alpha$.

Figure 2 shows the axial and radial velocity profiles for $Re_R = 10^{-2}$ (fixed value in all simulations) for $\chi = 1$ and $\eta = 2$. It can be observed that the alternance of slip and no slip boundary conditions determines, by flow incompressibility, a significant positive radial velocity component that pushes solute particles close to the slip wall (at the entrance of the gap zone) and a significant negative radial velocity component at the entrance of the pillar zone that pushes solute particle away from the no-slip wall. Axial flow variations, as well as radial secondary cross-flow are responsible for a significant reduction of solute dispersion.

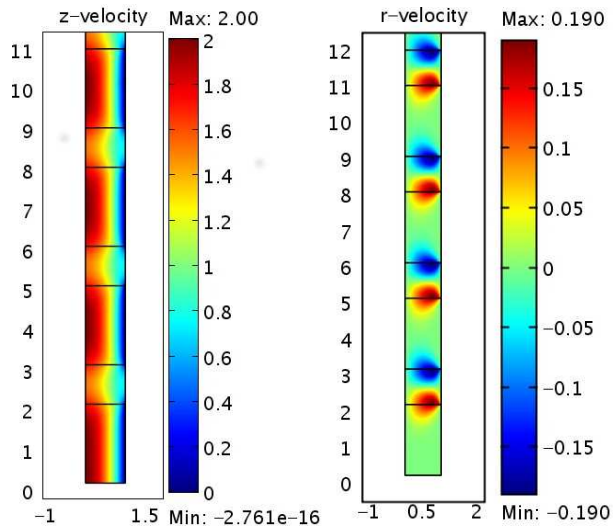

Figure 2. Axial v^*_ζ (left) and radial v^*_ρ (right) dimensionless velocity profiles for a patterned microchannel, $\chi = 1$, $\eta = 2$, $Re_R = 10^{-2}$.

Dispersion properties in a patterned microchannel can be investigated by analyzing the space-time evolution of the non-dimensional concentration of a solute impulsively injected into the microchannel at time $t = 0$, i.e. $\phi(\zeta = 0) = \delta(t)$. An impul-

sive injection means that the inlet concentration pulse duration should be much smaller than the flow residence time L/U.

In chromatographic experiments, one measures the average outlet profile $\langle\phi_{\rm out}\rangle(\tau)$ at the outlet section $\langle\phi_{\rm out}\rangle(\tau) = \int_0^1 \phi_{\rm out}(\rho,\tau)2\rho d\rho$, τ being the dimensionless time $\tau = tU/L$ (the physical time rescaled with respect to the flow residence time) and a compact quantitative description of $\langle\phi_{\rm out}\rangle(\tau)$ is provided by its temporal moments $m^{(n)}_{\rm out} = \int_0^\infty \tau^n \langle\phi_{\rm out}\rangle(\tau)d\tau$.
For $n = 1$, $m^{(1)}_{\rm out}$ corresponds to the dimensionless mean residence time while the second order moment $m^{(2)}_{\rm out}$ quantifies solute dispersion.
Specifically the second order central moment $\sigma^2_{\rm out} = m^{(2)}_{\rm out} - (m^{(1)}_{\rm out})^2$ is the typical measure of dispersion in chromatography and the effective dimensionless dispersion coefficient $D_{\rm eff}$ can be evaluated from $\sigma^2_{\rm out}$ as $\sigma^2_{\rm out} = \frac{2}{Pe_{\rm ax}} D_{\rm eff}$ where $Pe_{\rm ax} = UL/D$.
In a patterned microtube, the space-time evolution of the dimensionless solute concentration obeys the following balance equation and boundary conditions (Danckwertz outlet boundary condition is usually adopted for finite length-channels)

$$\frac{\partial\phi}{\partial\tau} = -\alpha \mathbf{v}^* \cdot \tilde{\nabla}\phi + \frac{\alpha}{Pe_R}\tilde{\nabla}^2\phi\,, \quad Pe_R = \frac{UR}{D} = \frac{Pe_{ax}}{\alpha} \tag{3}$$

$$\phi|_{\zeta=0} = \delta(\tau)\,, \quad \left.\frac{\partial\phi}{\partial\zeta}\right|_{\zeta=\alpha} = 0\,, \quad \left.\frac{\partial\phi}{\partial\rho}\right|_{\rho=0,1} = 0 \tag{4}$$

However, instead of solving a time dependent PDE for solute concentration ϕ, the analysis of dispersion can be equivalently and more efficiently approached by considering spatial behaviour of the temporal moments of ϕ and specifically the local moments $m^{(n)}(\zeta,\rho)$ and the average outlet moments $m^{(n)}_{\rm out}$ at the outlet ($\zeta = \alpha$) of the flow channel.

$$m^{(n)}(\zeta,\rho) = \frac{1}{\pi}\int_0^\infty \tau^n \phi(\zeta,\rho,\tau)\,d\tau\,,\; m^{(n)}_{\rm out} = \int_0^1 m^{(n)}(\alpha,\rho)2\pi\rho d\rho \tag{5}$$

The local moment hierarchy satisfies the following system of equations and boundary conditions

$$\alpha \mathbf{v}^* \cdot \tilde{\nabla} m^{(0)} = \frac{\alpha}{Pe_R}\tilde{\nabla}^2 m^{(0)}\,,\; m^{(0)}(0,\rho)| = 1/\pi \tag{6}$$

$$\alpha \mathbf{v}^* \cdot \tilde{\nabla} m^{(n)} = \frac{\alpha}{Pe_R}\tilde{\nabla}^2 m^{(n)} + n m^{(n-1)}\,,\; m^{(n)}(0,\rho) = 0 \tag{7}$$

$$\partial m^{(n)}/\partial\rho|_{\rho=0,1} = 0\,, \quad \partial m^{(n)}/\partial\zeta|_{\zeta=\alpha} = 0 \tag{8}$$

For infinitely extended channels Taylor-Aris theory provides a complete description of the dispersion properties. However, whenever finite length channels are considered, new dispersion features arise, associated with dispersion regimes that deviate from the Taylor-Aris predictions for high values of Pe_R.

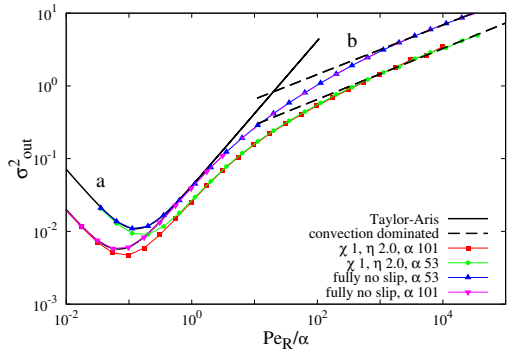

Figure 3. $\sigma^2_{\rm out}$ vs Pe_R/α for a fully noslip and a patterned microtube ($\chi = 1, \eta = 2$) for two aspect ratios $\alpha = 53, 101$. Continuous black curves (a) correspond to Taylor-Aris dispersion regime, Eq. (9). Black broken lines (b) correspond to the asymptotic scaling $\sigma^2_{\rm out} \sim (Pe_R/\alpha)^{1/3}$ (convection-dominated dispersion regime).

NUMERICAL RESULTS ON PATTERNED MICROCHANNELS

Figure 3 shows the behaviour of $\sigma^2_{\rm out}$ vs Pe_R/α for a fully no-slip finite-length channel ($\alpha = 53$ and $\alpha = 101$, long-thin channels) and the comparison with the Taylor-Aris prediction

$$\sigma^2_{\rm out} = \frac{2}{Pe_{\rm ax}} D^{TA}_{\rm eff} = \frac{2}{Pe_{\rm ax}}(1 + 4\Gamma_{\rm TA} Pe_R^2)\,, \quad \Gamma_{\rm TA} = 1/192. \tag{9}$$

It can be observed that from $Pe_R/\alpha \simeq 10$, the behavior of $\sigma^2_{\rm out}$ becomes practically independent of the aspect ratio α (as a consequence of the fact that the effect of axial diffusion becomes practically negligible) and the outlet variance starts to deviate from the Taylor-Aris scaling (which is linear in Pe_R), while for $Pe_R/\alpha > 10^3$ a fully developed different dispersion regime sets in [4; 5], associated with the asymptotic power-law scaling $\sigma^2_{\rm out} \sim (Pe_R/\alpha)^{1/3}$, characteristic of no-slip channels with smooth cross-section, circular in this specific case.
In the latter parameter region, the effect of axial convection becomes predominant, and consequently this transport regime can be referred to as *the Convection-dominated dispersion regime*. The excellent agreement between numerical results and theoretical behaviours in the whole range of Pe_R values supports the reliability of numerical simulations performed, at least in the fully no-slip case.
A similar dispersion behavior is also observed for the variance of the outlet concentration in a patterned microchannel with $\chi = 1, \eta = 2$. Also in this case we observe that the outlet variance $\sigma^2_{\rm out}$ exhibits a minimum and a then a linear behaviour (Taylor-Aris dispersion regime for $Pe_R/\alpha < 10$) and then a transition towards the asymptotic $1/3$ power-law convection-dominated scaling behavior. The asymptotic scaling, for very large values of Pe_R, is actually controlled by the fact that the capillary is characterized by an outlet no-slip section of length $2R$.

Fugure 4 shows the sensitivity of numerical results to the number of finite elements N_{FE} adopted in the numerical scheme. The mesh adopted $N_{FE} \geq 2 \times 10^6$ guarantees accuracy and reliability of numerical results in the whole range of Pe_R values analyzed.

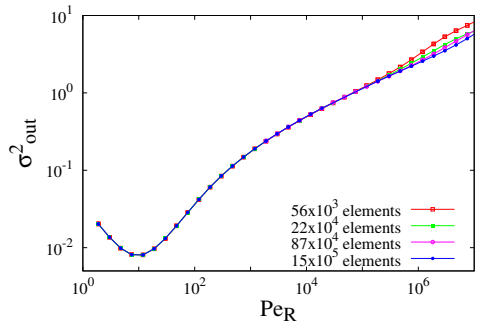

Figure 4. σ^2_{out} vs Pe_R for a patterned microtube ($\chi = 1, \eta = 1$, $\alpha = 53$) for increasing numbers of triangular elements adopted.

The global effect of the presence of gaps, and therefore of slip boundary conditions, is to lower dispersion in the whole range of Pe_R values analyzed. Figure 5 shows the behaviour of the ef-

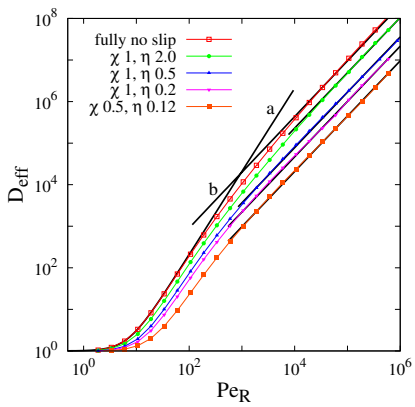

Figure 5. D_{eff} vs Pe_R for a fully no-slip and for different patterned microtubes. $\alpha = 53$. Curve (a) represents the Taylor-Aris behaviour, Eq.(9) for a no-slip channel. Curve (b) and its parallel lines represent the asymptotic behaviour $D_{\text{eff}} \sim Pe_R^{(1+1/3)}$.

fective dispersion coefficient $D_{\text{eff}} = \sigma^2_{\text{out}} Pe_{\text{ax}}/2$ as a function of Pe_R for different patterned microtubes characterized by different values of χ and η. It can be observed that, by decreasing the values of η, i.e. by decreasing the total no-slip pillar length, D_{eff} decreases in the whole range of Pe_R values and the asymptotic convection dominated dispersion regime, characterized by a power-law scaling $D_{\text{eff}} \sim Pe_R^{(1+1/3)}$ settles down from lower values of Pe_R.

TAYLOR-ARIS DISPERSION REGIME, $Pe_R < 100$

By focusing on the Taylor-Aris dispersion regime $Pe_R < 100$, in order to identify an equivalent slip-length, we compare the numerical results for D_{eff} for $Pe_R < 100$ with the Taylor-Aris

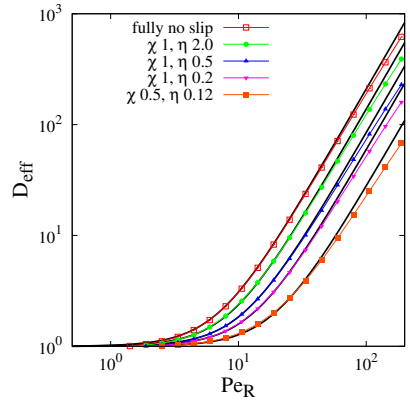

Figure 6. Comparison between numerical data for D_{eff} ($Pe_R < 100$) and the best fit curves (black lines) $D_{\text{eff}} = 1 + 4\Gamma_{\text{BF}}(\chi,\eta)Pe_R^2$ for different patterned microchannels.

dispersion coefficient in a microtube characterized an axial slip velocity profile (uniform along the axial coordinate ζ)

$$v^*_\zeta(\rho,\gamma) = \frac{2(1-\rho^2+2\gamma)}{1+4\gamma}\,, \quad v^*_w(\gamma) = v^*_\zeta(1,\gamma) = \frac{4\gamma}{1+4\gamma} \tag{10}$$

γ being the dimensionless slip length, for which the Taylor-Aris effective dispersion coefficient attains the form [1]

$$D_{\text{eff}} = 1 + 4\Gamma_{\text{TA}} Pe_R^2\,,\ \Gamma_{\text{TA}} = \frac{1}{192(1+4\gamma)^2} = \frac{(1-v^*_w(\gamma))^2}{192} \tag{11}$$

thus recovering the classical value $\Gamma_{\text{TA}} = 1/192$ for $\gamma = 0$ (no slip flow).

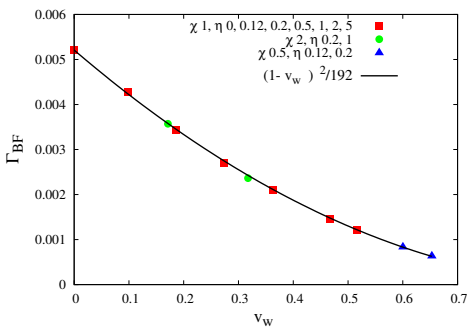

Figure 7. Comparison between best fit values $\Gamma_{\text{BF}}(\chi,\eta)$ vs the average axial wall velocity $\langle v^*_w \rangle$ for different patterned microtubes, $\alpha = 53$ and the analytic expression $\Gamma_{\text{TA}} = (1-\langle v^*_w \rangle)^2/192$.

Figure 6 shows the comparison between numerical results D_{eff} vs $Pe_R < 100$ and the best fit curves with $D_{\text{eff}} = 1 + 4\Gamma_{\text{BF}}(\chi,\eta)Pe_R^2$, supporting the idea that the patterned microtube, in the Taylor-Aris dispersion regime, can be regarded as a microtube with an axial slip velocity profile, each microtube, depending on the value of χ and η, characterized by a different value of

$\Gamma_{TA} = \Gamma_{\mathrm{BF}}(\chi,\eta)$.
Figure 7 shows the behaviour of the best fit values $\Gamma_{\mathrm{BF}}(\chi,\eta)$ vs the average wall velocity $\langle v_w^* \rangle = \frac{1}{\alpha}\int_0^\alpha v_\zeta^*(\zeta,\rho=1)d\zeta$ for different patterned microchannels characterized by different values of χ and η and the excellent agreement with the theoretical prediction Eq. (11) by simply replacing $v_w^*(\gamma)$ with $\langle v_w^* \rangle$.

This implies that a patterned microchannel, characterized by a given value of χ and η and therefore by a given and easily computed $\langle v_w^* \rangle$ exhibits the same effective dispersion coefficient, in the Taylor-Aris dispersion regime, as a fully slip microtube, of the same aspect ratio α and the same slip wall velocity, i.e. $v_w^*(\gamma) = \langle v_w^* \rangle$ and therefore characterized a slip length $\gamma = \frac{1}{4}\langle v_w^* \rangle/(1-\langle v_w^* \rangle)$.

CONVECTION DOMINATED REGIME, $Pe_R > 100$

For higher values of Pe_R, in order to quantify the effective decrease of the dispersion coefficient (with respect to the fully no-slip case) due to the patterned structure of the microchannel, we analyze the prefactor β of the asymptotic behavior $D_{\mathrm{eff}} = \beta Pe_R^{(1+1/3)}$ evaluated from best fits of curves reported in Figures 3-5 and other numerical simulations not reported here for sake of brevity. Also in this case, we characterize each microchannel in

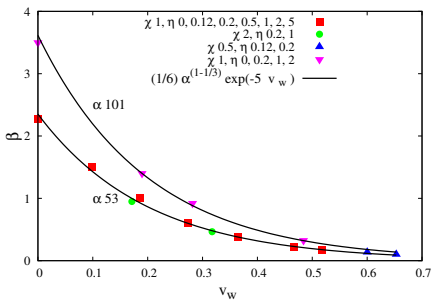

Figure 8. Prefactor β of the convection-dominated power-law behaviour $D_{\mathrm{eff}} = \beta Pe_R^{(1+1/3)}$ for different patterned microchannels and two different aspect ratios $\alpha = 53, 101$.

terms of its characteristic average wall velocity $\langle v_w^* \rangle$.

Figure 8 shows the behaviour of β vs $\langle v_w^* \rangle$ for different patterned microchannels characterized by an inlet and a outlet no-slip zones of length $2R$, different values of χ, η and different aspect ratios $\alpha = 53, 101$. It can be easily observed that the prefactor β, and therefore D_{eff}, decreases exponentially with $\langle v_w^* \rangle$ i.e. $D_{\mathrm{eff}} = (1/6)\alpha^{(1-1/3)}\exp(-5\langle v_w^* \rangle)$, with an heuristic exponent -5, while it increases with the aspect ratio α with a power-law $\alpha^{(1-1/3)} = \alpha^{2/3}$ simply deriving from the fact that, for $Pe_R/\alpha > 10$ the curves σ^2_{out} vs Pe_R/α become practically independent of the aspect ratio α, see Figure 3.

Moreover, in order to further pursue the analogy between patterned and slip microtubes that we successfully verified in the Taylor-Aris regime, we focused on two reference patterned microchannels, with the same aspect ratio $\alpha = 53$, namely microtube M1 with $\chi = 1$ and $\eta = 5$ (very small average wall velocity $\langle v_w^* \rangle = 0.098$ and few axial changes of the velocity field) and microtube M2 with $\chi = 1$ and $\eta = 0.2$ (higher average wall velocity $\langle v_w^* \rangle = 0.467$ and very frequent axial changes of the velocity field). Then, for each of the two reference microchannels M1 and M2, we numerically computed the velocity field and the effective dispersion coefficient (in the whole range of Pe_R values) of a microchannel characterized by an inlet and outlet no-slip zones of length $2R$ and a central part of length $\alpha - 4$ with a uniform axial slip velocity at the channel wall $v_\zeta^*(\zeta,1) = v_s^* = \langle v_w^* \rangle \alpha/(\alpha-4)$ in such a way to have a slip microchannel with the same average wall velocity $\langle v_w^* \rangle$ of the corresponding patterned microchannel.
Figure 9 shows the excellent agreement between D_{eff} vs Pe_R for

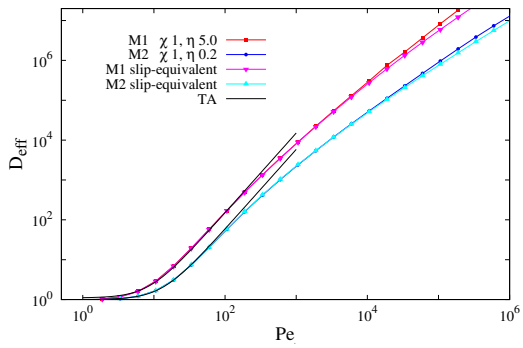

Figure 9. D_{eff} vs Pe_R for the reference microchannels M1 and M2 and for the corresponding slip-equivalent microchannels characterized by the same average wall velocity. Continuous black lines represent the corresponding Taylor-Aris behaviour, the same as reported in Figure 6.

the reference microchannels M1 and M2 and for the corresponding slip-equivalent microchannels characterized by the same average wall velocity. The slip-equivalent microchannel exhibits the same dispersion features as the patterned microchannel in the whole range of Pe_R values: the same Taylor-Aris behavior for $Pe_R < 100$ (in perfect agreement with what we observed in the previous section), the same transitional behaviour at intermediate Pe_R values towards the asymptotic convection dominated power-law scaling.
This can be better clarified by observing the spatial (axial) behaviour of the pointwise variance $\sigma^2_\zeta(\zeta)$

$$\sigma^2_\zeta(\zeta) = \int_0^1 m^{(2)}(\zeta,\rho)2\pi\rho d\rho - \left(\int_0^1 m^{(1)}(\zeta,\rho)2\pi\rho d\rho\right)^2 \quad (12)$$

corresponding to σ^2_{out} for $\zeta = \alpha$, i.e. at the outlet section.
Figures 10 A-B show the behaviour of $\sigma^2_\zeta(\zeta)$ for three increasing values of $Pe_R = 10^3, 10^4, 10^4$ for the patterned (blue continuous line) and for the slip-equivalent (red lines with dots) microtubes.

By focusing on the patterned microchannel, the spatial behaviour of σ^2_ζ clearly shows how the variance increases along the pillars, exhibits a sudden decrease at the pillar-gap interface and a sudden increase at the gap-pillar transition zone. These spa-

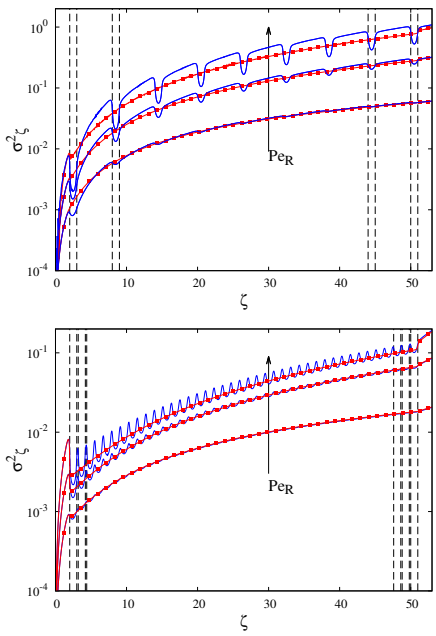

Figure 10. $\sigma^2_\zeta(\zeta)$ vs ζ for $Pe_R = 10^3, 10^4, 10^4$, $\alpha = 53$. Comparison between patterned (blue lines) and slip-equivalent (red dotted lines) microchannels M1 ($\chi = 1$, $\eta = 5$ (TOP)) and M2 ($\chi = 1$, $\eta = 0.2$ (BOTTOM)). Vertical broken lines highlight the transition zones from gaps to pillars and viceversa.

tial oscillations, becoming more and more evident for increasing values of Pe_R, are "averaged out" by the spatial behaviour of σ^2_ζ for the corresponding slip-equivalent microchannel, still retaining all the quantitative features of the corresponding patterned microchannel.

Small differences in the dispersion behaviour between patterned and slip-equivalent microchannels can be observed only for very high values of Pe_R, namely for $Pe_R > 10^5$, and these differences are more pronounced for microchannel M1 than M2. This phenomenon can be easily explained by considering that, at very high Peclet numbers, dispersion features are highly sensitive to small differences in the velocity field in the proximity to the outlet section.

By focusing on the last gap-pillar interface at $\zeta = \alpha - 2$, for the patterned microchannel M1, the axial wall velocity $v^*_\zeta(\zeta, 1)$ jumps down from a maximum value $v^*_\zeta(\zeta, 1) = 0.734$ (in the center of the last gap) to zero in the last outlet pillar. This jump is significantly larger than the axial velocity jump from $v^*_s = 0.107$ to 0 at the last gap-pillar interface, $\zeta = \alpha - 2$, for the corresponding slip-equivalent microchannel. This explains why, the pointwise variance $\sigma^2_\zeta(\zeta)$ for M1 exhibits a sudden and significant increase at the gap-pillar interface $\zeta = \alpha - 2$, that is definitely more pronounced (at $Pe_R = 10^5$) than that observed for the corresponding slip-equivalent microchannel, thus resulting in an outlet variance (and therefore effective dispersion coefficient) for M1 higher than the corresponding slip-equivalent microchannel.

For the patterned microchannel M2, the wall velocity jump at $\zeta = \alpha - 2$ is $\Delta = 0.743$ for M2 and $\Delta = 0.504$ for the slip-equivalent microchannel. Therefore the pointwise variance $\sigma^2_\zeta(\zeta)$ exhibits a similar increase at $\zeta = \alpha - 2$ for M2 and its slip-equivalent microchannels, thus resulting in closer values of the outlet variance and effective dispersion coefficient even for very high Peclet values, $Pe > 10^5$.

CONCLUSIONS

We analyzed solute dispersion in a finite-length patterned channel by considering the temporal moments of solute concentration and specifically the local temporal moments and the average moments at the outlet of the flow channel. With this approach it has been possible to investigate the dispersion properties at low and high Peclet numbers.

We investigated both the Taylor-Aris and the convection dominated dispersion regimes, by analyzing dispersion feature in the wide range of cross-sectional Peclet values $Pe_R \in [1 - 10^6]$.

We have shown and quantified how the patterned structure of the microchannel and the alternance between slip and no-slip boundary conditions, depending on geometrical parameters χ and η, significantly affects (actually reduces) solute dispersion in finite-length channels.

We have shown that, in the whole range of Peclet values, the dispersion features of a patterned microchannel are equivalent to the dispersion properties of a slip-equivalent microchannel exhibiting the same wall average velocity.

This implies that two patterned microchannels, different in gaps and pillars position and length, but characterized by the same average wall velocity, exhibit the same dispersion features.

REFERENCES

[1] Chiu-On Ng, How does wall slippage affect hydrodynamic dispersion? , *Microfluid Nanofluid*, Vol. 10, 2011, pp 47-57.

[2] A. Adrover, S. Cerbelli, F. Garofalo and M. Giona, Convection-Dominated Dispersion Regime in Wide-Bore Chromatography: A Transport-Based Approach To Assess the Occurrence of Slip Flows in Microchannels, *Anal. Chem.*, Vol 81, 2009, pp 80098014.

[3] Ajdari A., Bontoux N. and Stone H.A., Hydrodynamic Dispersion in Shallow Microchannels: the Effect of Cross-Sectional Shape, *Anal. Chem*, Vol. 78, 2006, pp 387-392.

[4] M. Giona, A. Adrover, S. Cerbelli, and F. Garofalo, Laminar dispersion at high Pclet numbers in finite-length channels: Effects of the near-wall velocity profile, *Physics of Fluids*, Vol 21, 2009, 123601.

[5] A. Adrover, Effect of secondary flows on dispersion in finite-length channels at high Peclet numbers, *Phys. Fluids*, Vol 25, 2013, 093601.

[6] Cassie A.B.D. and Baxter S., Wettability of porous surfaces, *Trans. Faraday Society*, Vol 40, 1944, pp 546-551. 20

[7] Lauga E. and Stone H.A., Effective slip in pressure-driven Stokes flow. *J. Fluid Mech.*,Vol 489, 2003, pp 55-77.

[8] Aris R., On the dispersion of a solute in a fluid flowing through a tube, *Proc. R. Soc. Lond. A*, Vol 235, 1956, pp 6777.

[9] S.K. Bhaumik, A. Kannan and S. DasGupta, Taylor-Aris dispersion Induced by axial variation in velocity profile in patterned microchannels, *Chem. Eng. Sci.*, Vol 134, 2015, pp 251-259.